




High-order parametric generation of coherent XUV radiation: supplement

O. HORT,^{1,2,3,*}  A. DUBROUIL,^{1,4} M. A. KHOKHLOVA,^{5,6} D. DESCAMPS,¹  S. PETIT,¹ F. BURG,¹ E. MÉVEL,¹ E. CONSTANT,^{1,7}  AND V. V. STRELKOV^{8,9}

¹Université de Bordeaux, CNRS, CEA, Centre Laser Intenses et Applications (CELIA), 43 rue P. Noailles, 33400 Talence, France

²Photonics Institute, Vienna University of Technology, Gusshausstraße 27, A- 1040 Vienna, Austria

³ELI Beamlines, FZU – Institute of Physics of the Czech Academy of Sciences, Na Slovance 1999/2, 182 21 Praha 8, Czech Republic

⁴Currently with Femtoeasy, Femto Easy SAS, Bât. Gienah, Cité de la Photonique, 11 avenue de Canteranne, 33600 Pessac, France

⁵Max Born Institute for Nonlinear Optics and Short Pulse Spectroscopy, Max-Born-Straße 2A, Berlin 12489, Germany

⁶Blackett Laboratory, Imperial College London, South Kensington Campus, London SW7 2AZ, United Kingdom

⁷Université de Lyon, Université Claude Bernard Lyon 1, CNRS, Institut Lumière Matière (ILM), 69622 Villeurbanne, France

⁸Prokhorov General Physics Institute of the Russian Academy of Sciences, 38 Vavilova Street, Moscow 119991, Russia

⁹Moscow Institute of Physics and Technology (State University), Dolgoprudny, Moscow Region 141700, Russia

*ondrej.hort@eli-beams.eu

This supplement published with The Optical Society on 9 February 2021 by The Authors under the terms of the [Creative Commons Attribution 4.0 License](https://creativecommons.org/licenses/by/4.0/) in the format provided by the authors and unedited. Further distribution of this work must maintain attribution to the author(s) and the published article's title, journal citation, and DOI.

Supplement DOI: <https://doi.org/10.6084/m9.figshare.13762018>

Parent Article DOI: <https://doi.org/10.1364/OE.418449>

High-order parametric generation of coherent XUV radiation: supplemental document

This document provides supplementary information to “High-order parametric generation of coherent XUV radiation.” In the following, we offer additional experimental results to support the conclusions in the main text and to demonstrate the robustness of the parametric process. Technical details of the experimental setup and simulation are also provided.

1. EXPERIMENTAL SETUP

To perform the experiment we used a chirped-pulse amplification (CPA) based Ti:Sapphire laser chain delivering multi-mJ TW pulses of 45 fs duration centered at 810 nm at a repetition rate of 10 Hz. The beam was spatially filtered by a hollow core capillary. The Strehl ratio was measured by a wavefront sensor (HASO) giving the value of 0.95. The collimated IR beam with $w = 10$ mm radius at $1/e^2$ was clipped by an iris of 22 mm diameter before being focused by a mirror of focal length of 2 m into a gas jet with a focus spot of $w = 73$ μm radius at $1/e^2$ (corresponding to a Rayleigh length of 21 mm). Note that this generation geometry favors the detection of the short quantum trajectory only. The nozzle of the gas jet is 250 μm in diameter leading to a 0.8 mm medium length in the laser interaction region. The back pressure of krypton gas was around 3 bars. Estimates for the medium length (0.8 mm) and for the pressure in the interaction zone (100 – 150 mbar) have been done within a gas density measurement technique similar to [1].

The generated XUV radiation was then spectrally and spatially resolved by a flat field spectrometer consisting of 0.5 mm entrance slit imaged by a 3° grazing-incidence Hitachi concave grating (1200 gr/mm) onto 40-mm-diameter dual multi-channel plates (MCP) coupled to a phosphor screen. The resolution of the spectrometer is estimated to be 0.26 eV for HH21, 0.27 eV for HH31 and 0.33 eV for HH43. The XUV signal is therefore measured behind the slit that is centered on the beam axis. All data presented are only corrected from background signal of the detector. The horizontal continuous line in the lower part of the krypton and argon spectra is caused by a diffusive reflection of low harmonic orders in a vacuum tube between the XUV grating and the MCP detector and therefore has no significance for the results.

In such conditions the XUV radiation is generated in a loose-focusing regime where the generating medium is much thinner than the Rayleigh range of the driving beam. One should note that the XUV signal is high enough to acquire the spatially resolved spectra on a single-shot basis (see Figures S3 and S6), although for better statistics the presented spectra were acquired as 10 shots average.

We stress that using loose focusing and spatially filtered beam together with acquiring high-resolution spatially-resolved spectra with wide spectral range facilitate greatly the recognition of such phenomena as HPG rather than HHG.

The values of IR pulse intensity are estimated for vacuum (linear) propagation of the laser beam. During the laser pulse propagation in the medium, when the gas is ionized, the rise in intensity is not directly corresponding the vacuum propagation case due to the plasma defocusing and the peak intensity can even decrease.

2. SIMULATION DESCRIPTION

The microscopic response is calculated via numerical solution of the 3D time-dependent Schrödinger equation (TDSE) for a model single-active electron atom in external field. This microscopic polarization is used in the propagation equation to calculate the macroscopic response. However, the full numerical integration of the 3D propagation equation is very heavy. Consequently, we split it into two parts. Within the first part we study the THz field generation near the beam axis, using very high peak intensities achieved on axis in our experiments. In contrast to majority of the studies of the THz field generation, we focus on the THz field *inside* the generating medium. We solve the 1D propagation equation:

$$\frac{\partial E_\omega(z)}{\partial z} = - \frac{i2\pi\omega}{c} P_\omega(z),$$

where E_ω is a field slowly-varying spectral amplitude at the frequency ω , P_ω is the slowly-varying spectral amplitude of the polarization of the medium which is proportional to the gas density and the single-atom response calculated via 3D TDSE (the numerical approach for the TDSE solution is described in [2]). The equation is solved numerically by a slice-by-slice propagation: the field found at an n^{th} slice is used in the TDSE solution to calculate the polarization and thus the field at the next $(n+1)^{\text{th}}$ slice (the details of the numerical approach for the propagation equation integration are described in [3]).

In these calculations we find that the THz radiation with frequencies of about 20 – 30 THz can be efficiently generated in our conditions.

At the second stage of our calculations we study XUV generation in the laser and THz field. Complete simulation of our experimental conditions exceeds our numerical capabilities, so we deal with shorter propagation distances, lower harmonic orders and the THz field with somewhat higher frequency of $2/17\omega_0$. Moreover, we consider the laser intensity that is lower than at the beam axis, taking into account that the periphery of the laser beam with such a level of intensity has relatively high volume and that such intensities are favorable for HHG.

Note, that our approach of the macroscopic response calculation based on polarization calculated via TDSE solution is exact (within 1D propagation and single-active electron approximation), so it includes processes of HHG, high-order frequency mixing, HPG, plasma blue shift of the generating and generated waves, and so on.

3. XUV SIGNAL PRESSURE DEPENDENCE

The evolution of the XUV spectra as a function of generating medium pressure was acquired via changing the delay time between the driving pulse and the nozzle opening time. The zero delay denotes the optimal time synchronization used for acquisition of data presented in Figures 1–3 in the main text. The positive delay means that the nozzle opens after the optimal time, meaning that the gas has not yet fully reached the interaction zone and the driving laser pulse interacts with lower gas pressure. In the negative delay the laser pulse interacts with the lower gas pressure because the nozzle is closing and the gas jet is already spreading into the vacuum chamber. In such a way, one can effectively and accurately change the gas pressure in the interaction zone. The experimental results were acquired using the driving laser intensity $3.5 \times 10^{15} \text{ Wcm}^{-2}$ in the same conditions as for Figure 1 in the main text and are presented in Figure S1 for several delays.

Figure S1 presents the evolution of the HHG and HPG signal in the regime of high intensity, making the HH peaks very blue-shifted and spatially irregular as discussed in the main text. The HPG signal rises when the time synchronization approaches the optimal value. However, neither the RSS beam shape nor the spectral frequency depend on the gas pressure.

4. XUV SPECTRA GENERATED IN VARIOUS GASES AND INTERACTION GEOMETRIES

Figures S2 - S6 present the experimental spatially-resolved XUV spectra generated in various gases and interaction geometries to demonstrate the robustness of the HPG signal in different experimental conditions. The y-axis represents the spatial divergence in mrad and the colorbar indicates spatio-spectral intensity (in arbitrary units). The photon energy $q\omega_0$ of the HH are presented by the solid white lines, while the photon energy of the RSS given by Equation (1) are shown by dashed lines.

We present XUV spectra generated in krypton, argon and neon jets. Figures S2 - S5 present only harmonic orders of 21 - 47 while similar characteristics of the XUV radiation are shown for low orders of 17 - 21 in Figure S6. Higher orders than 47 are not directly detectable due to the geometry of the XUV spectrometer.

Figure S2 expands the dataset shown on Figure 1 in the main text comparing the spatially-resolved XUV spectra for more values of driving laser intensity.

Figure S3 shows the XUV spectrograms generated in argon jet in similar experimental conditions to Figure S2 and Figure 1 in the main text but with lower driving laser intensity.

Figure S4 shows the XUV spectrograms generated in neon jet in the same experimental conditions as Figure S2.

Figure S5 shows the XUV spectrograms generated in krypton jet with lower driving intensity corresponding to the gas jet position 15 mm after the focal spot. Other experimental conditions are similar to those in Figure S2.

Figure S6 shows the XUV spectrograms generated in argon jet in similar experimental condi-

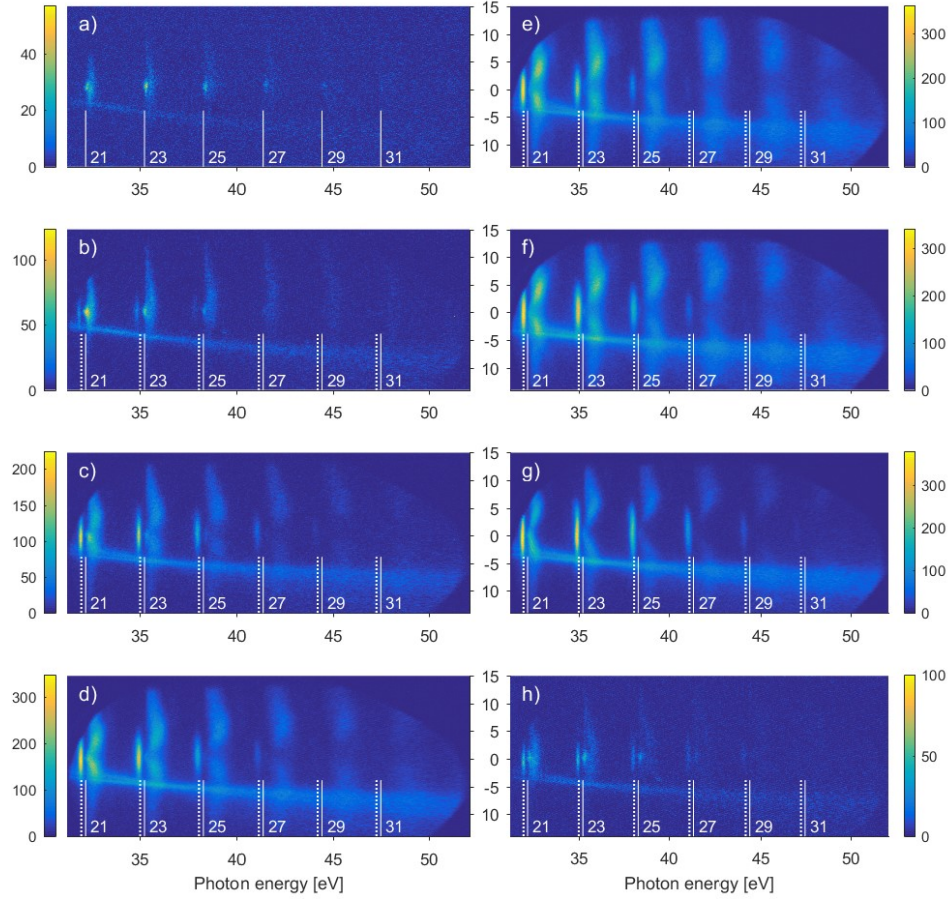


Fig. S1. Experimental spatially-resolved XUV spectra generated in krypton jet. The y-axis represents the spatial divergence (in mrad) and the colorbar spatio-spectral intensity (in arbitrary units). The photon energies $q\omega_0$ of the HH are presented by the solid white lines, while the photon energies of the RSS given by Equation (1) with the parameters $Q = 27$ and $m = -2$ are shown by dashed lines. The driving laser intensity is $3.5 \times 10^{15} \text{ Wcm}^{-2}$ and the pulsed valve opening is delayed by (from a to h) -30, -20, -10, 0, 10, 20, 30 and 40 μs to change the gas pressure.

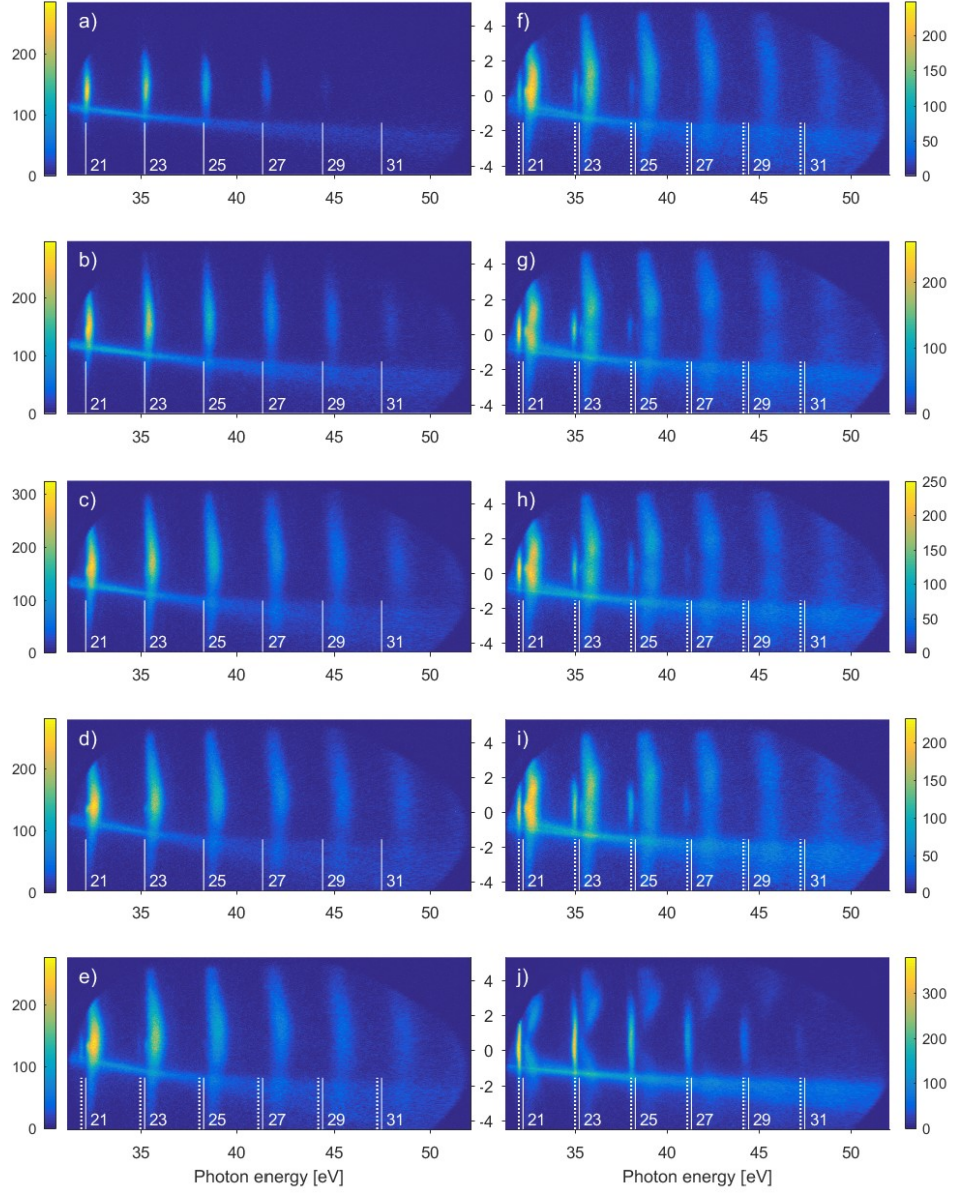


Fig. S2. Experimental spatially-resolved XUV spectra generated in a krypton jet. The parameters of Equation (1) are $Q = 27$ and $m = -2$. The driving laser intensities are $0.15, 0.38, 0.71, 1.1, 1.6, 2.1, 2.5, 2.9, 3.2$ and $3.5 \times 10^{15} \text{ Wcm}^{-2}$ from a to j.

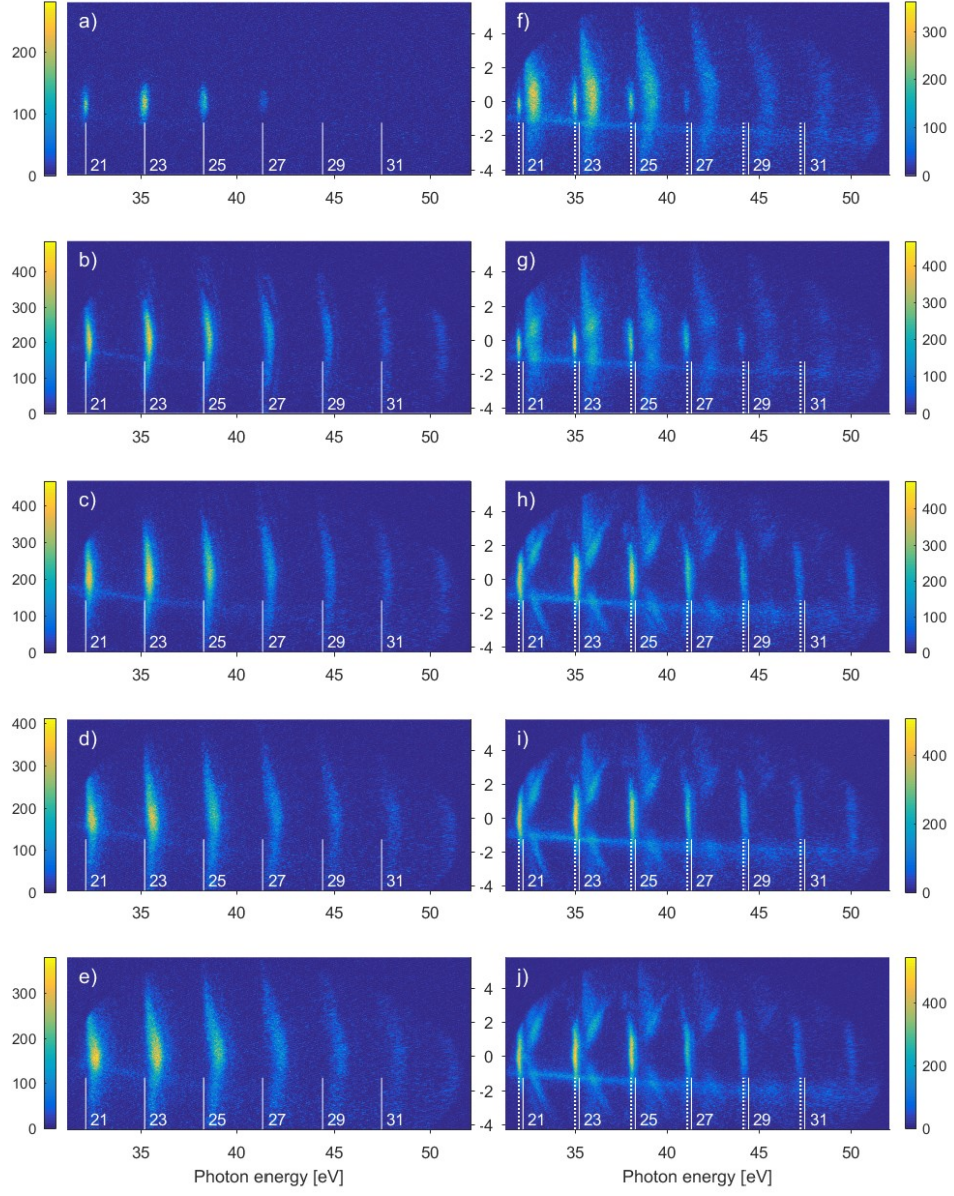


Fig. S3. Experimental spatially-resolved XUV spectra generated in argon jet. The parameters of Equation (1) are $Q = 27$ and $m = -2$. The driving laser intensities are 0.09, 0.15, 0.25, 0.38, 0.53, 0.91, 1.1, 1.6, 1.8 and $2.3 \times 10^{15} \text{ Wcm}^{-2}$ from a to j.

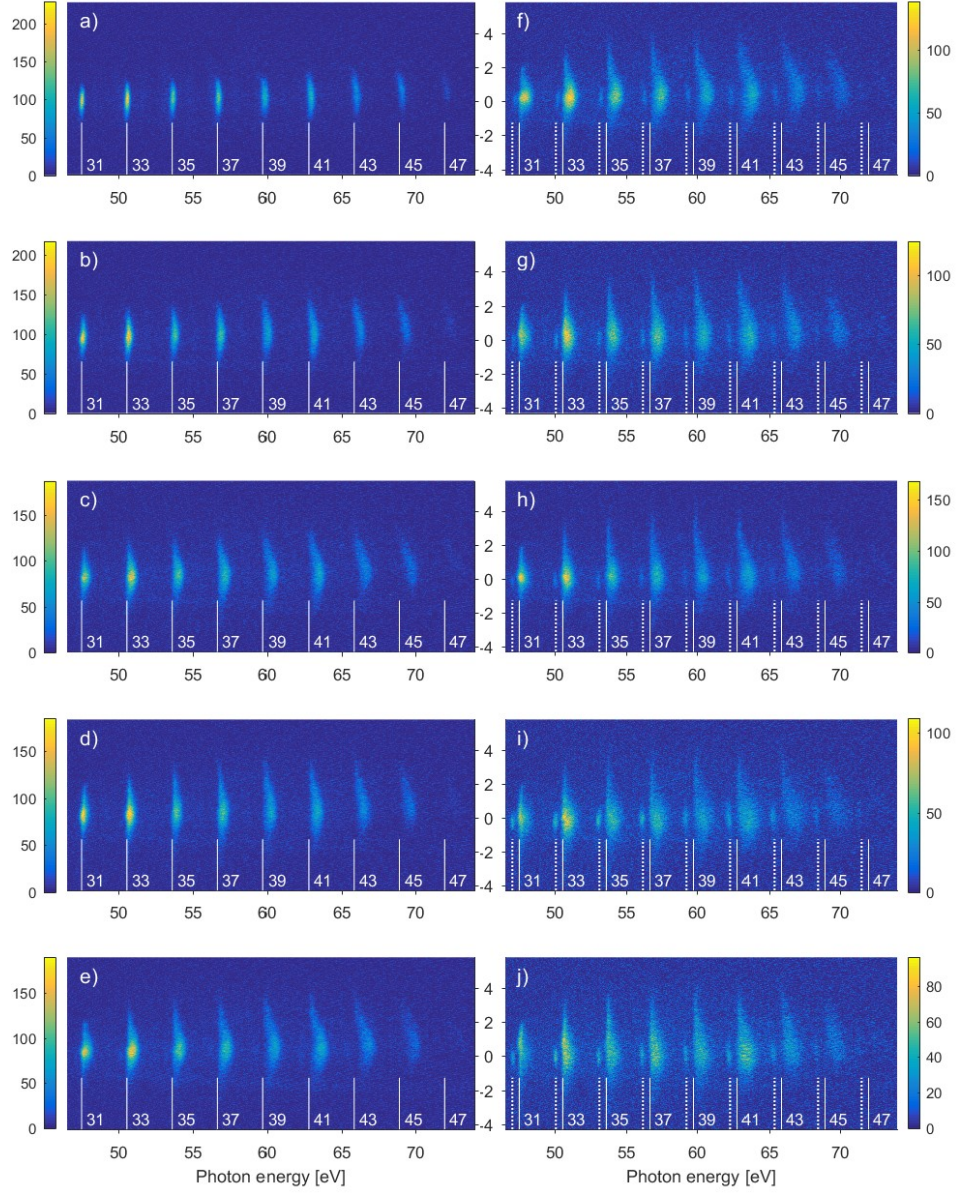


Fig. S4. Experimental spatially-resolved XUV spectra generated in neon jet. The parameters of Equation (1) are $Q = 25$ and $m = -4$. The driving laser intensities are 0.38, 0.71, 1.1, 1.6, 2.1, 2.5, 2.9, 3.2, 3.4 and $3.5 \times 10^{15} \text{ Wcm}^{-2}$ from a to j.

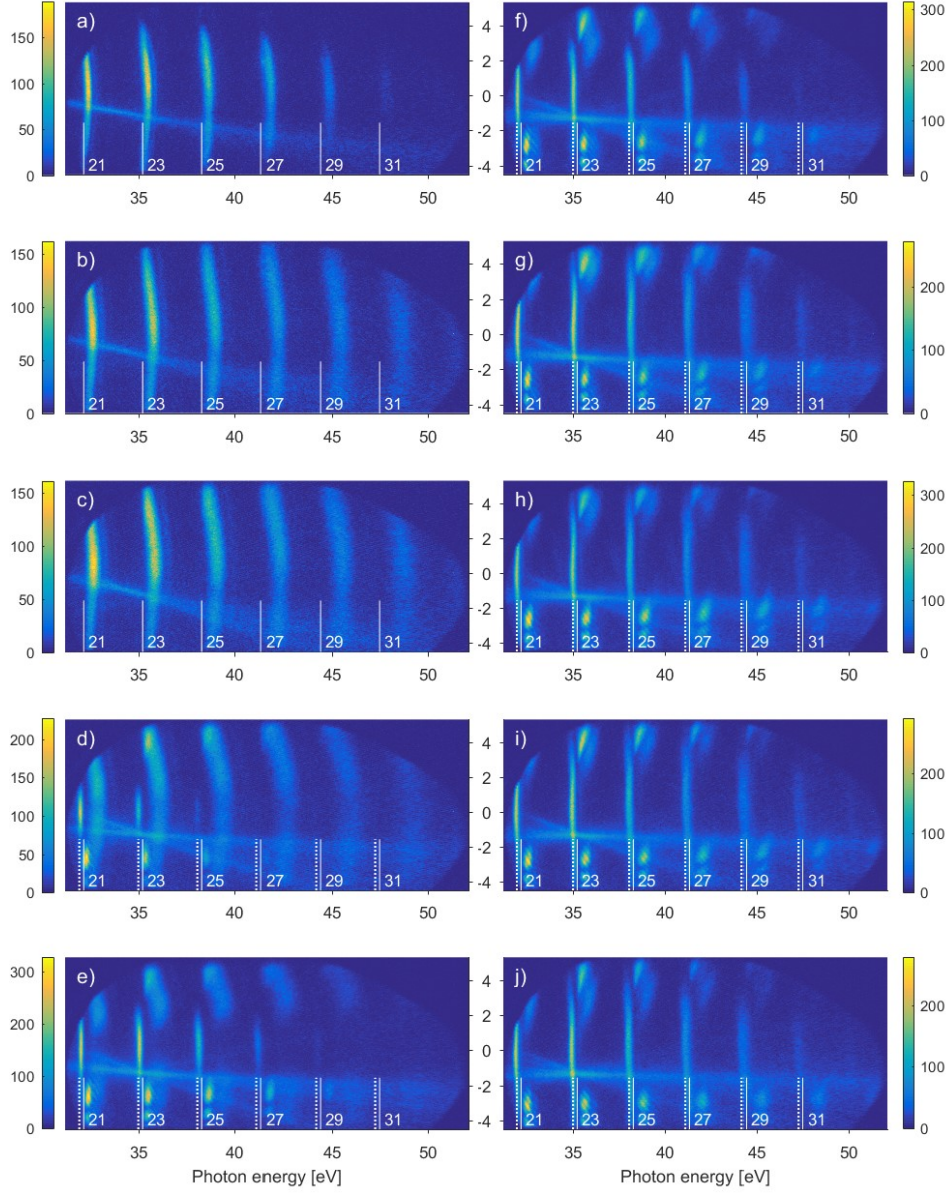


Fig. S5. Experimental spatially-resolved XUV spectra generated in krypton jet located 15 mm after the focal spot. The parameters of Equation (1) are $Q = 27$ and $m = -2$. The driving laser intensities are 0.12, 0.29, 0.55, 0.87, 1.2, 1.6, 2.0, 2.5, 2.65 and $2.7 \times 10^{15} \text{ Wcm}^{-2}$ from a to j. tions to Figure S2 but the spectrometer was set to detect harmonic orders 17 - 21. Therefore, it is complementary spectral range to Figure S3.

Overall, these observations show that the HPG process is robust and occurs in many different experimental conditions, once the laser intensity is high enough.

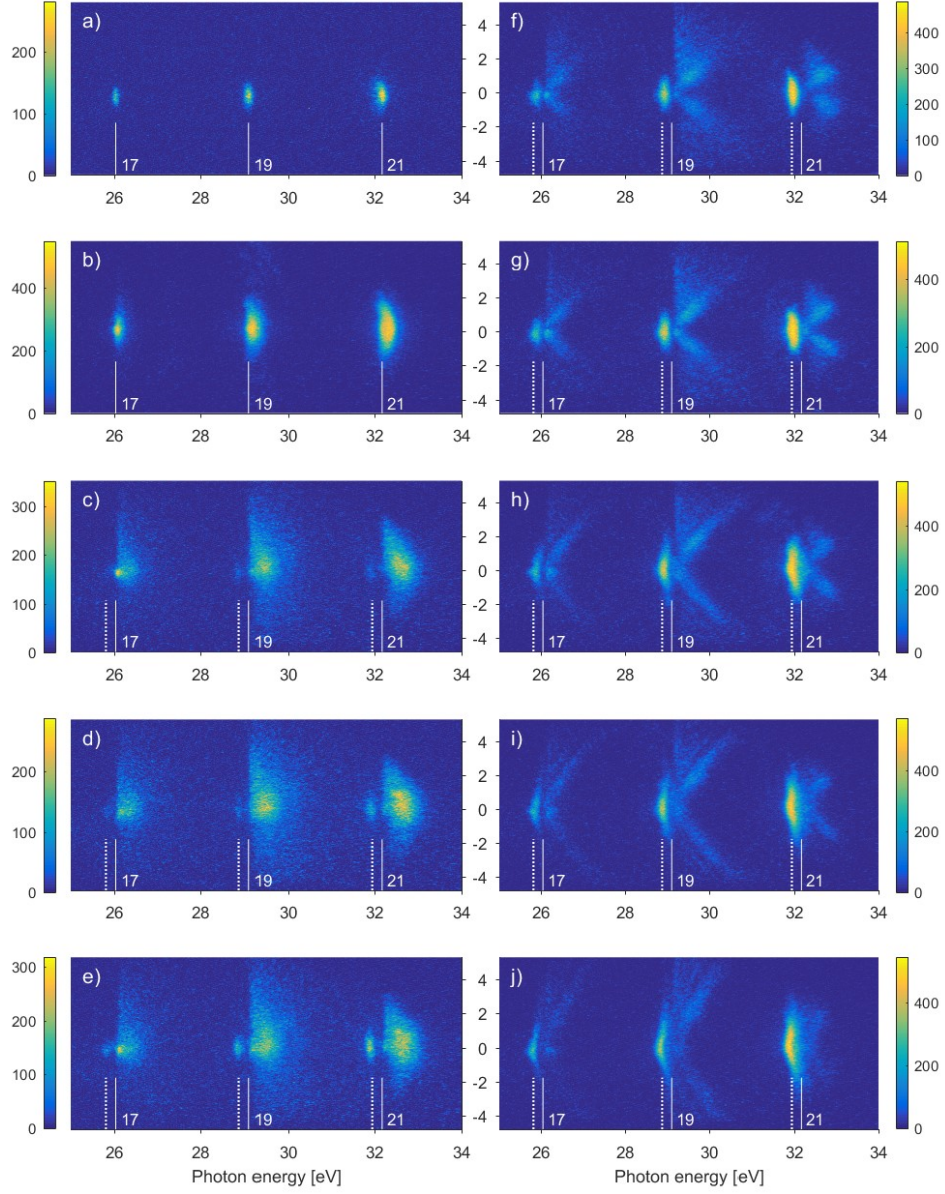


Fig. S6. Experimental spatially-resolved XUV spectra generated in argon jet. The parameters of Equation (1) are $Q = 27$ and $m = -2$. The driving laser intensities are 0.09, 0.25, 0.71, 0.91, 1.1, 1.4, 1.8, 2.5, 2.7 and $3.1 \times 10^{15} \text{ Wcm}^{-2}$ from a to j.

REFERENCES

1. A. Comby, S. Beaulieu, E. Constant, D. Descamps, S. Petit, and Y. Mairesse, "Absolute gas density profiling in high-order harmonic generation," *Opt. express* **26**, 6001–6009 (2018).
2. V. Strelkov, A. Sterjantov, N. Y. Shubin, and V. Platonenko, "Xuv generation with severalcycle laser pulse in barrier-suppression regime," *J. Phys. B: At. Mol. Opt. Phys.* **39**, 577–589 (2006).

M. Khokhlova and V. Strelkov, "Highly efficient XUV generation via high-order frequency mixing," *New J. Phys.* **22**, 093030 (2020).